ELSEVIER

Journal of the Mechanics and Physics of Solids
51 (2003) 2213–2237

JOURNAL OF THE
MECHANICS AND
PHYSICS OF SOLIDS

www.elsevier.com/locate/jmps

Determination of mechanical properties of carbon nanotubes and vertically aligned carbon nanotube forests using nanoindentation

H.J. Qi[a], K.B.K. Teo[b], K.K.S. Lau[c], M.C. Boyce[a,*], W.I. Milne[b], J. Robertson[b], K.K. Gleason[c]

[a] *Department of Mechanical Engineering, Massachusetts Institute of Technology, Cambridge, MA 02139, USA*

[b] *Department of Engineering, University of Cambridge, Cambridge, CB2 1PZ, UK*

[c] *Department of Chemical Engineering, Massachusetts Institute of Technology, Cambridge, MA 02139, USA*

Dedicated to L.B. Freund on the occasion of his 60th birthday

Abstract

Vertically aligned carbon nanotubes (VACNT) have been a recent subject of intense investigation due to the numerous potential applications of VACNTs ranging from field emission and vacuum microelectronic devices to the creation of super-hydrophobic surfaces and as a source of well defined CNTs. In this paper, a new method to determine the mechanical properties of VACNT and constituent nanotubes using nanoindentation tests is proposed. The study of nanoindentation on a VACNT forest reveals a process whereby nanotubes are consecutively bent during the penetration of the indentor. Therefore, the resistance of a VACNT forest to penetration is due to successive bending of nanotubes as the indentor encounters nanotubes. Using a micro-mechanical model of the indentation process, the effective bending stiffness $(EI)_{\text{eff}}$ of constituent nanotubes in the VACNT array is then deduced from nanoindentation force-penetration depth curves. A simple method accounting for the multiwalled structure of multiwall nanotubes is used to interpret the obtained $(EI)_{\text{eff}}$ in terms of an effective bending modulus E_t^{b}, an effective axial modulus E_t^{a}, and a wall modulus E_t^{w} of a nanotube. Nanoindentation tests on three VACNT forest samples reveal the effective bending modulus of multiwall carbon nanotubes to be $E_t^{\text{b}} = 0.91 \sim 1.24$ TPa, and effective axial modulus to be $E_t^{\text{a}} = 0.90$–1.23 TPa. These values are in good agreement with tests conducted on isolated MWCNTs. Taking the mechanical wall thickness to be 0.075 nm, the nanotube wall modulus is found to be $E_t^{\text{w}} = 4.14$–5.61 TPa, which is in good agreement with predictions from atomic simulations. The use of nanoindentation together with the proposed micromechanical model of the successive bending of nanotubes as the

*Corresponding author. Tel.: +1-617-253-2342; fax: +1-617-258-8742.
E-mail address: mcboyce@mit.edu (M.C. Boyce).

0022-5096/$ - see front matter
doi:10.1016/j.jmps.2003.09.015

indentor penetrates into the forest is hereby shown to result in a novel approach for determining not only the dependence of the indentation resistance on the key structural features of the forest (CNT diameter, length and areal density), but also provides a measure of the stiffness of the constituent carbon nanotubes. This new technique requires no special treatment of the samples, making it promising to apply this method to a large number of tests to determine the statistical properties of CNTs, and implying the potential use of this method as a quality control measurement in mass production.

Keywords: A. Nanoindentation; Mechanical Properties; B. Multiwalled Carbon Nanotubes; Vertically Aligned Carbon Nanotubes; Nanofibers

1. Introduction

Carbon nanotubes (CNTs) are a subject of intensive investigations due to their remarkable electrical and mechanical properties (Baughman et al., 2002). CNTs exist in one of two forms: Single-walled carbon nanotubes (SWCNTs) or multi-walled carbon nanotubes (MWCNTs), and can be further classified by their chirality (the wrapping angle of the hexagonal atomic thin layer). The primary methods used to produce CNTs are carbon-arc discharge, laser ablation of graphite, and chemical vapor deposition (CVD). In many applications, it is desirable that CNTs have well defined diameters and lengths so that the properties of CNTs can be readily tailored for their applications. Recently, plasma enhanced chemical vapor deposition (PECVD) has been used to grow forest-like vertically aligned carbon nanotubes (VACNTs) onto substrates coated with a suitable metal catalyst (Huang et al., 1998, 2002; Chhowalla et al., 2001; Han et al., 2002). There is presently great interest in VACNTs for field emission and vacuum microelectronic devices, as well as for the creation of super-hydrophobic surfaces and as a technique for producing well defined CNTs. Compared with the efforts focused on optimizing the PECVD growth conditions, however, little attention has been given to the mechanical properties of these forests even though the stiffness and mechanical integrity will be important issues in their ultimate success.

Due to the nanometer scale of dimensions, it is a challenge to experimentally measure mechanical properties of CNTs. The first measurement of the elastic modulus of CNTs was conducted by Treacy et al. (1996) whereby the amplitude of thermally-induced vibrations of isolated nanotubes was measured within a TEM; classical beam theory, where the nanotubes were idealized as solid rods, was then used to calculate the modulus. The effective bending modulus derived from this method ranged from 0.4 to 4.15 TPa with 1.8 TPa as an average value over 11 CNTs. In addition to the large range in the value of the elastic modulus, this method is also limited by the requirement that the vibration of nanotubes must be neither too high nor too small for TEM detection. Wong et al. (1997) dispersed MWCNTs on a smooth flat surface and pinned the nanotubes by the deposition of an array of square pads on this substrate. An AFM was then used to scratch the surface at the “free” end of the nanotube and the lateral force and displacement were measured. Beam theory, assuming a solid cross section,

was then used to reduce the data, yielding a modulus of MWCNTs 1.28 ± 0.59 TPa. It should be noted that although adhesive and frictional forces might increase scratching resistance, they were neglected in their method. Salvetat et al. (1999) deposited CNTs on a well polished alumina ultra-filtration membrane, on which a CNT occasionally laid over a pore. The tube was then subjected to bending using nanoindentation. The effective bending modulus from this method was found to be 0.81 ± 0.41 TPa. These three techniques, each providing bending modulus measurements on individual nanotubes, require complicated preparations before the measurements can be conducted. In these methods, the effective bending modulus E_t^{b} is determined using beam theory whereby an effective bending stiffness $(EI)_{\mathrm{eff}}$ is measured and the modulus is then determined assuming an effective moment of inertia $I_{\mathrm{eff}} = \pi(D_{\mathrm{o}}^4 - D_{\mathrm{i}}^4)/64$, where D_{o} is the outer diameter and D_{i} is the inner diameter. Furthermore, this is approximated as $I_{\mathrm{eff}} \approx \pi D_{\mathrm{o}}^4/64$, since D_{i} is typically much smaller than D_{o}. The modulus is then computed to be

$$E_t^{\mathrm{b}} \approx \frac{(EI)_{\mathrm{eff}}}{I_{\mathrm{eff}}}. \tag{1}$$

In this paper, nanoindentations on VACNT forests will be shown to provide a measure of the indentation resistance of a nanotube forest coating as well as a statistical measure of the effective bending stiffness $(EI)_{\mathrm{eff}}$ and effective bending modulus E_t^{b} of MWCNTs when combined with a simple analytical model of nanoindentation tests. Further reduction of the results, which account for the nested tube structure of a MWCNT, enables the calculations of a wall modulus and a tube axial modulus. Below, descriptions of the materials and the experimental procedure are first presented. A model of the behavior of VACNT forests during nanoindentation is then presented and is used together with tests to determine the average bending stiffness, bending modulus, wall modulus, and axial modulus of the constituent nanotubes in the VACNT forests studied. Nanoindentation is thus shown to be an excellent new technique to measure both the indentation resistance of VACNT forests and the elastic modulus of individual constituent CNTs.

2. Experimental procedure

2.1. Materials

Three vertically aligned carbon nanotube forest samples were prepared at University of Cambridge using PECVD (Plasma Enhanced Chemical Vapor Deposition) method (Chhowalla et al., 2001) with different nickel catalyst thickness (ranging from 3.5 to 7 nm) and growth time. The samples were then studied at MIT under a JOEL SEM, with the samples tilted by 0° (observed from top), 15°, and 25°. Fig. 1 shows images where samples were tilted by 25° so that the forest-like landscapes of the VACNTs were clearly depicted. The areal density measurement for each sample was conducted by counting the number of nanotubes in the image, then dividing the total number of nanotubes by the total area of the image; measurements were made on images with

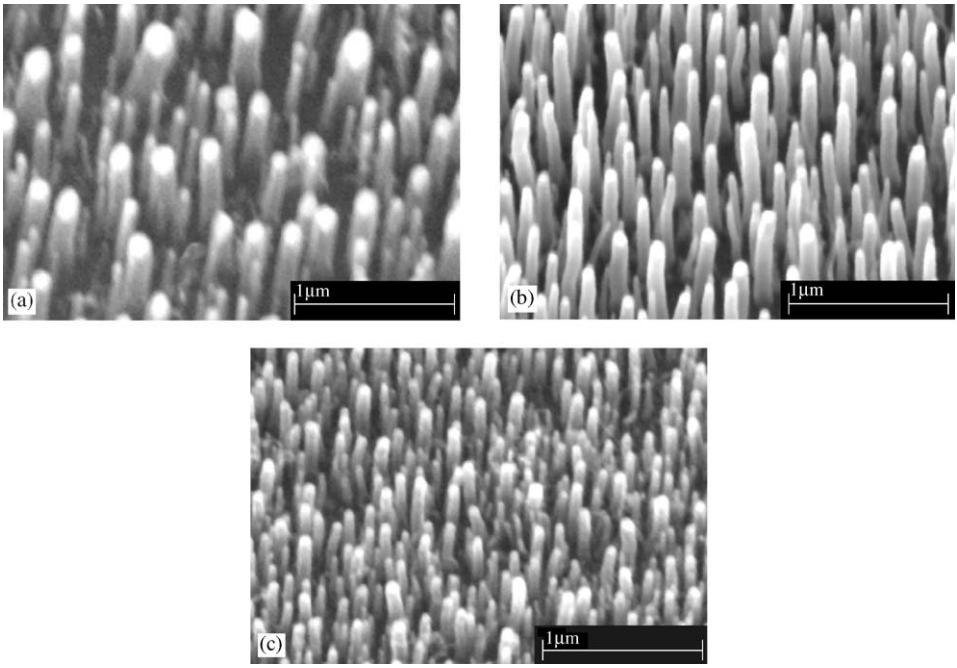

Fig. 1. Vertically aligned carbon nanotubes: (a) Sample A; (b) Sample B; and (c) Sample C. The samples are tilted by 25° to reveal the forest-like landscapes.

Table 1
Dimensions of the three VACNT samples

Sample	Outer diameter		Length		Areal density	
	Average D_o (nm)	Deviation σ_{D_o} (nm)	Average L (nm)	Deviation σ_L (nm)	m (μm^{-2})	Percentage of area covered by CNTs (%)
A	104	36	930	123	27	23
B	90	17	1150	160	26	17
C	55	13	570	107	40	10

the sample tilted by 0°, 15° and 25°, then averaged over these three measurements. The diameter and length were measured from images with the samples tilted by 0° (for diameter only), 15°, and 25°, respectively. For each image, at least 30 nanotubes were randomly selected for measurements. The length and diameter measurements were further verified by measuring nanotubes that had been laid flat on the substrate with a pair of tweezers. The average and deviation of diameter and length, and the areal density (number of tubes per μm^2 of substrate) for each of the three samples are listed in Table 1.

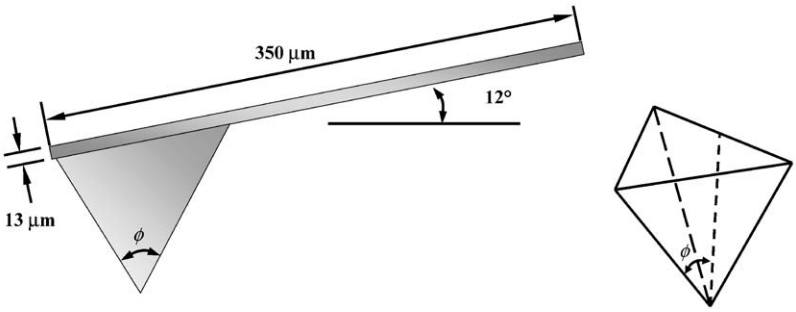

Fig. 2. Schematics of the geometry of the diamond tip of the nanoindentor.

2.2. Nanoindentation

Nanoindentation tests on VACNT forests were conducted at MIT using a Digital Instrument Dimension 3100 SPM (Scanning Probe Microscopy). The nanoindentation cantilever is made of stainless steel and has a diamond tip. The working resonant frequency is about 55 to 60 kHz in tapping mode. Fig. 2 shows a schematic of the geometry of the diamond tip and the cantilever (Digital Instrument, 1998). The diamond tip is a three-sided pyramid, with an apex angle $\phi = 60°$, measured from a face to an edge of the pyramid. According to the specification from the tip supplier, the radius of the diamond tip is less than 25 nm.

The standard procedure for nanoindentation tests within an AFM was followed. The tapping mode is first engaged to scan the surface and the area of interest is located. When nanoindentation is initiated, the tip is lifted slightly (typically about 100–300 nm) above the surface. As the nanoindentation is executed, the tip is driven by the piezo-scanner toward the surface until a pre-set reaction force is reached. The tip is then retracted back to its initial position.

Fig. 3 shows a typical indentation force-penetration curve ($f-p$ curve) for a nanoindentation test on a VACNT forest sample. The indentation force starts from zero until a certain penetration depth is reached, then grows in a nonlinear manner where the slope of the curve increases as the penetration depth increases.

3. A model based on beam theory and statistics

3.1. Physical process of nanoindentation on VACNT forest

When the pyramidal diamond tip indents into the VACNT forest, individual nanotubes are subjected to bending deformation. Fig. 4 illustrates this process with a 2D schematic, where the tip is depicted as a wedge with a semi-apex angle of θ. Only two nanotubes are shown in the figure sequences for the sake of brevity. The lengths of the nanotubes are L. The tip is initially located a distance h_0 above the top surface

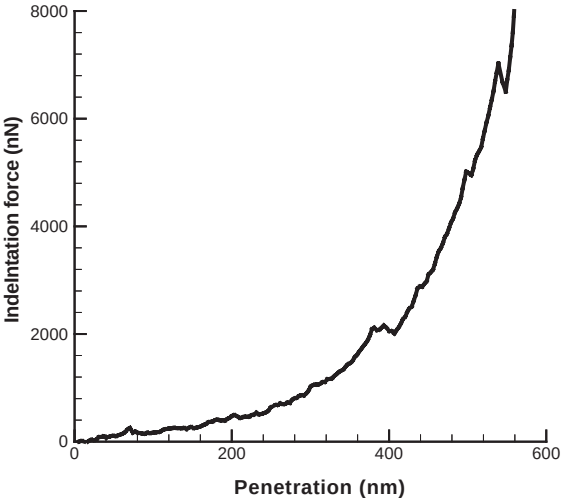

Fig. 3. Typical indentation force-penetration curve ($f-p$ curve) during nanoindentation of VACNT forest.

of the nanotubes (Fig. 4(a)). In Fig. 4, the penetration h is measured from the top level of VACNT forest, and $h+h_0$ gives the total travel distance of the indentor. The value of h_0 will vary from test to test and is determined using the method outlined in Appendix A. As the tip is driven towards the substrate surface, at a certain penetration depth of h_1, a surface of the indentor encounters a nanotube (Fig. 4(b)). This first nanotube then bends as the indentor penetration depth increases; at a certain penetration depth of h_2, the indentor surface encounters a second nanotube (Fig. 4(c)). This process continues until a pre-set maximum force is reached. The tip then retracts back to its original position. The indentation force vs. penetration depth curve ($f-p$ curve) can be predicted using the model presented below.

3.2. The consecutive contact model

When a nanotube is in contact with the indentor, (see the free body diagram of Fig. 5), the bending deflection at the tip of the nanotube can be estimated using beam theory and is related to the indentation force P_i and lateral force T_i by (see Appendix B for the formulation):

$$w_0 = \frac{T_i}{P_i}\left(\frac{\tan k_i L}{k_i} - L\right), \tag{2}$$

where $k_i = \sqrt{P_i/(EI)_{\text{eff}}}$. $(EI)_{\text{eff}}$ is the effective bending stiffness of a nanotube in the VACNT forest and is the variable to be determined. The deflection w_0 of the nanotube is related to the geometry of the indentor and the depth of penetration; it is

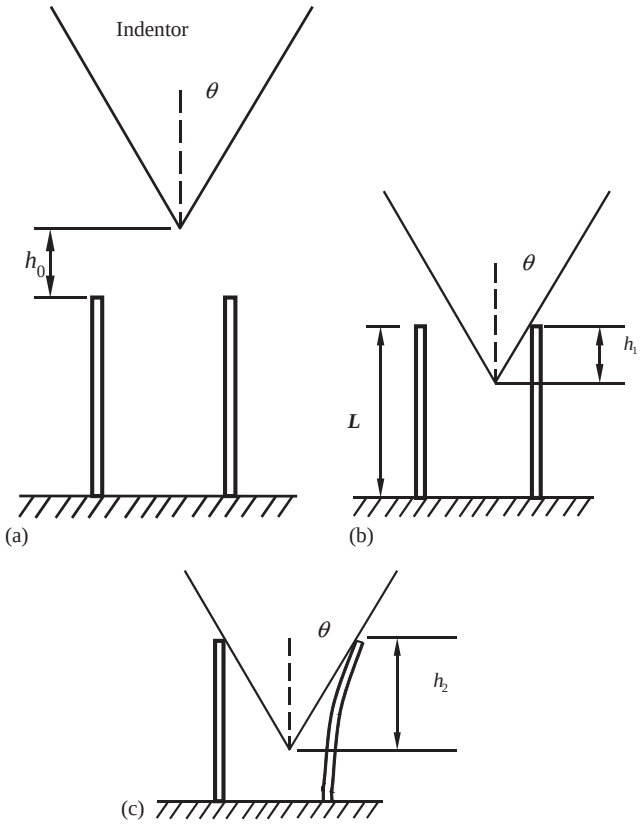

Fig. 4. Schematics of consecutive contacts of the indentor and nanotubes in a nanoindentation test (a) before the nanoindentation; (b) the tip encounters one nanotube; and (c) the tip encounters two nanotubes.

given by

$$w_0 = (h - h_i)\tan\theta, \tag{3}$$

where h is the penetration depth of the indentor, h_i is the penetration at which the ith nanotube is touched by the tip. Assuming any frictional force at the contact surface can be neglected gives

$$\frac{P_i}{T_i} = \tan\theta. \tag{4}$$

Then, combining Eqs. (2)–(4), a nonlinear relationship between penetration depth h and indentation force P_i for a single nanotube is obtained

$$h = h_i + \frac{1}{(\tan\theta)^2}\left(\frac{\tan k_i L}{k_i} - L\right), \quad k_i = \sqrt{P_i/(EI)_{\text{eff}}}. \tag{5}$$

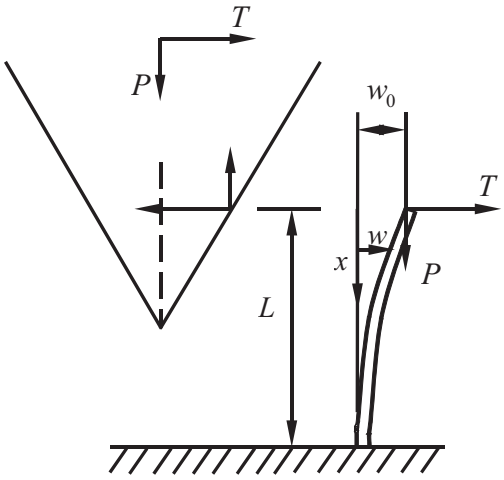

Fig. 5. Free body diagram of a nanotube touched by the indentor.

For the case where n nanotubes are in contact with the tip, the total indentation force P is given by

$$P = \sum_{i=1}^{n} \alpha_i P_i, \tag{6}$$

where $\alpha_i = 0$ when $h \leqslant h_i$, and $\alpha_i = 1$, when $h > h_i$. The parameters α_i and h_i can be determined through geometrical calculations.

As illustrated in Fig. 4, the value of h_i for an individual nanotube depends on the position of the indentor relative to the nanotube. Nevertheless, for a large number of indentation tests, the average value $\bar{h}_i$ for the ith contact can be calculated using statistical information about the VACNT. The diamond tip is a three-sided pyramid with an apex angle of 60° measured from a face to an edge of the pyramid. At a depth h, the area enclosing the cross-section of the indentor and a nanotube with diameter D_o (Fig. 6) is given by

$$A = 0.813h^2 + 4.110D_o h + 3.141D_o^2 \ (\mu m^2). \tag{7}$$

The nanotube areal density is denoted by m nanotubes per μm^2. Therefore, the average number i of nanotubes in contact with the indentor at a given depth $\bar{h}_i$ is given by

$$i = Am. \tag{8}$$

The effective bending stiffness $(EI)_{eff}$ is determined by best fitting the average of the $f-p$ curves from tests with theoretical predictions using Eqs. (5)–(8), where $(EI)_{eff}$ and h_0 are variables. The elastic modulus of the walls of a CNT and the effective bending

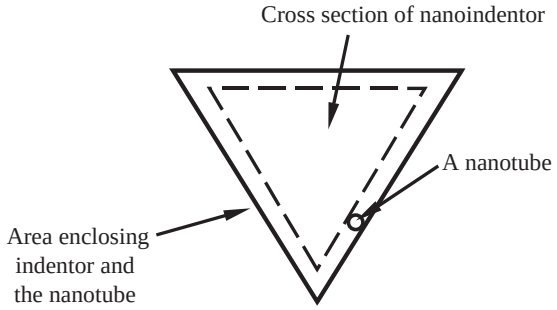

Fig. 6. Area enclosing the cross-sectional area of the indentor and a nanotube with diameter D_o.

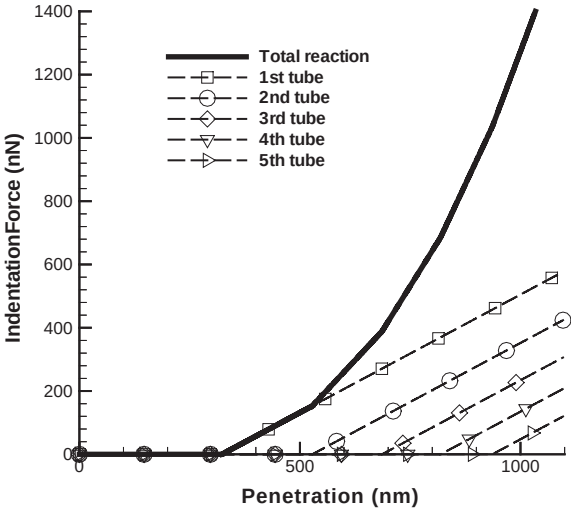

Fig. 7. Superposition of interactions between the indentor and nanotubes encountered by the indentor during nanoindentation gives the total penetration resistance. The thick line is the total resistance. The thin lines are the resistance forces from individual nanotubes.

modulus of the MWCNT can then be determined from $(EI)_{\text{eff}}$ and the geometry of the MWCNTs, as will be described later.

3.3. Example

We now consider the indentation of an example VACNT forest with nanotube diameter of 80 nm, length of 1100 nm, areal density $m = 5$ tubes/μm^2, and effective bending stiffness $(EI)_{\text{eff}} = 2.1\ \text{N(nm)}^2$. Nanotubes are randomly distributed over the substrate. Fig. 7 presents the average indentation force vs. penetration curve that would be measured for the nanoindentation tests and shows the force contributions from the successive interactions between the indentor and individual nanotubes.

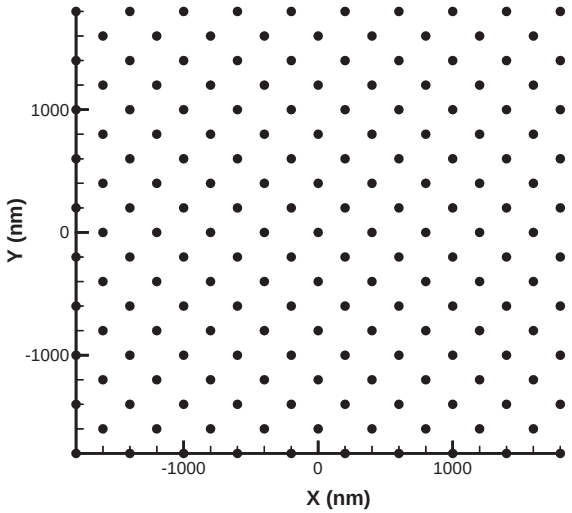

Fig. 8. A two dimensional FCC pattern of nanotubes.

The $f-p$ curve in Fig. 7 is also a representative curve and would vary depending upon the particular location of the indentation. In addition, there is typically a range in geometric features (diameter and length) of nanotubes in a VACNT forest. A statistically representative model can be achieved by generating a VACNT array, where positions, diameters, and lengths of nanotubes are varied in a statistical manner. Then, several indentations on such a VACNT are simulated and averaged to determine the indentation vs. penetration curve (Note that several curves are also experimentally measured and averaged). For the purpose of comparison and discussion, the prediction using average geometrical parameters will be denoted as the representative average simulation (RAS), while the simulations using random distributions of geometrical parameters will be referred to as statistical simulations.

3.4. Parametric studies: sensitivities of penetration resistance to geometrical parameters of VACNTs

Using the model of nanoindentation proposed above, the sensitivity of the indentation resistance curve to various geometrical parameters is examined, including the effects of indentation locations, spatial distribution of the CNTs, distribution in the diameter and length of the CNTs.

As discussed above, an individual $f-p$ curve depends on the location where the indentor penetrates into the VACNT forest. To further illustrate this effect, a two dimensional face centered cube (FCC) spatial distribution of nanotube positions is created with an areal density of $m = 12$ tubes/μm^2 (Fig. 8). The diameter and length of nanotubes are 80 and 1100 nm, respectively, and are taken to be identical for all nanotubes. $(EI)_{\text{eff}}$ is taken to be 2.1 N$(nm)^2$. Six nanoindentation tests are conducted numerically (Case 1), with indentation positions chosen deliberately (Fig. 9(a)).

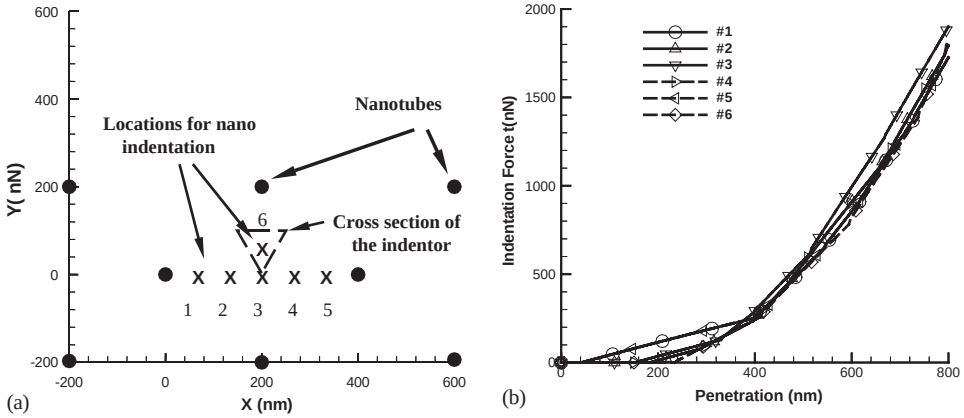

Fig. 9. Case 1: nanoindentations on a two dimensional FCC patterned VACNT forest, (a) locations of nanoindentations; and (b) $f-p$ curves.

The $f-p$ curves (Fig. 9(b)) for the indentations at positions 1 and 5, and 2 and 4, are identical, respectively, due to symmetry. The interaction between nanotubes and the indentor occurs first for the indentations at positions 1 and 5. Position 6 is deliberately chosen so that the indentation at this point encounters two nanotubes simultaneously at the first touch. Therefore, the initial slope of the indentation force-penetration curve for position 6 is twice that of other curves. It is also noted that the chosen indentation positions capture the overall variations in $f-p$ curves. Indeed, $f-p$ curves from numerical nanoindentation simulations with randomly chosen indentation positions showed no significant variation from those of Fig. 9(b).

To study the dependence of the indentation resistance of a VACNT forest on the distribution of nanotubes, the positions of nanotubes are allowed to vary randomly (Fig. 10(a)) on the substrate (Case 2), while areal density is retained to be about 12 tubes/μm^2. The length and diameter are taken to be the same values as those in the above study. 20 nanoindentations at randomly chosen positions are conducted, and Fig. 10(b) shows the $f-p$ curves from the first 6 nanoindentations for the sake of brevity. As expected, given the random distribution of nanotubes on the substrate, the indentation force-penetration curves show greater variation compared to the curves from nanoindentation on a regular FCC patterned nanotube forest. When nanotubes form a regular pattern, there is a limited variation in indentation locations relative to neighboring nanotubes and thus a limited variation in the number of CNTs that will be encountered as a function of penetration depth. In contrast, if nanotubes are randomly distributed, the occurrence of consecutive contacts is unpredictable and highly varied, especially for VACNT forests of low areal density. As the areal density increases, such variation is reduced.

Fig. 11 shows the effect of a distribution in lengths on the $f-p$ curves of a VACNT forest (Case 3). The nanotubes are spatially arranged in a two dimensional FCC pattern (Fig. 8). All nanotubes have identical diameter of 80 nm, but a Gaussian distribution in

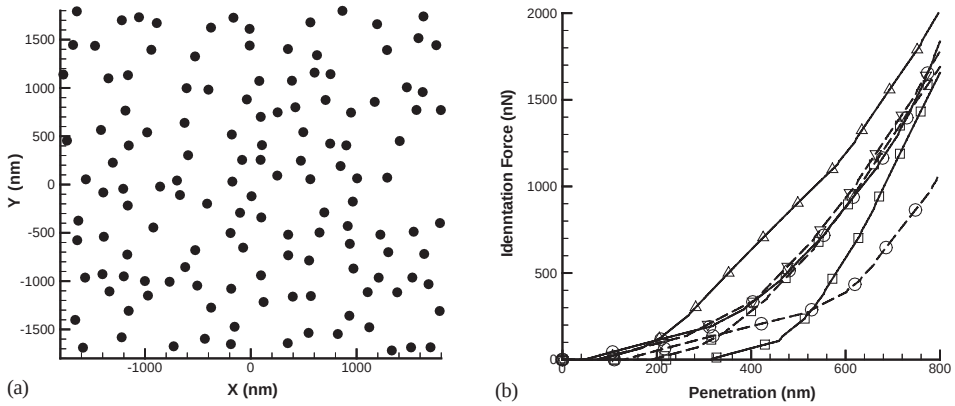

Fig. 10. Case 2: random nanoindentations on a VACNT forest where nanotubes are randomly distributed, (a) positions of nanotubes; and (b) $f-p$ curves.

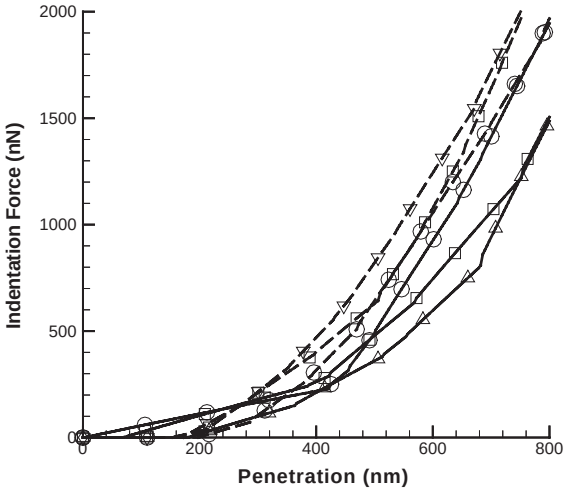

Fig. 11. Case 3: random nanoindentations on a VACNT forest where the nanotubes are distributed following a two dimensional FCC pattern, and all the nanotubes have identical diameter of 80 nm, but average length of 1100 nm with deviation of 20%.

lengths with an average length of 1100 nm and standard deviation of 20%. Compared with Fig. 9(b), where the lengths of nanotubes are fixed, the variation in length results in a significant scattering in the $f-p$ curves.

Fig. 12 shows the effect of a distribution in nanotube diameter on the nanoindentation of a VACNT forest (Case 4). The nanotubes are spatially arranged in a two dimensional FCC pattern (Fig. 8). All nanotubes have identical length of 1100 nm, but a Gaussian

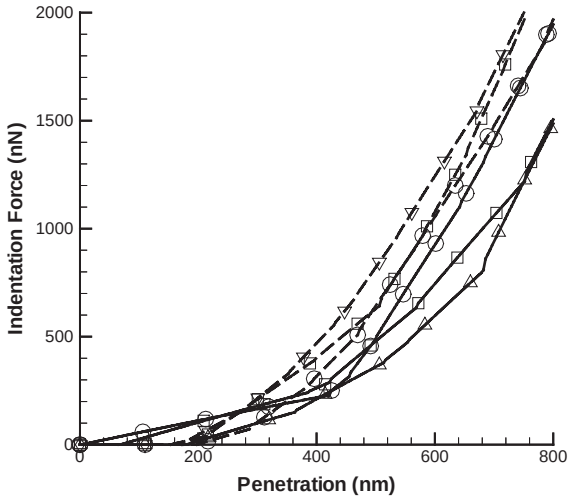

Fig. 12. Case 4: nanoindentations on a VACNT forest where the nanotubes are distributed following a two dimensional FCC pattern, and all the nanotubes have identical length of 1100 nm, but average diameter of 80 nm with deviation of 20%.

distribution in diameter with an average diameter of 80 nm and standard deviation of 20%. The effective bending stiffness for each nanotube is scaled through

$$(EI)_{\mathrm{eff},j} = (EI)_{\mathrm{eff}} \left(\frac{(D_{\mathrm{o}})_j}{\bar{D}_{\mathrm{o}}} \right)^4, \tag{9}$$

where $(EI)_{\mathrm{eff}} = 2.1\ \mathrm{N(nm)}^2$. The variation in diameter is seen to give a wider range in $f-p$ curves because of the fact that the standard deviation of 20% in D_{o} generates a higher deviation in $(EI)_{\mathrm{eff}}$ according to Eq. (9).

Fig. 13 shows the effect of a distribution in spatial positions, lengths and diameters on the nanoindentation of a VACNT forest (Case 5). The nanotubes are randomly distributed, and have a Gaussian distribution in length and diameter with average length of 1100 nm and average diameter of 80 nm, and standard deviation of 20% for both. As expected, the indentation force-penetration curves are significantly scattered.

Fig. 14(a) shows the average $f-p$ curves over 6 simulations for Case 1, and over 20 simulations for Cases 2–5. Although large scatters in $f-p$ curves for Case 2, 3 and 5 are observed, the average curves over 20 simulations converge to the representative average simulation (RAS). The only exception is Case 4, where the average $f-p$ curve shows a stiffer response than those predicted in other cases.

It is also noticed that the average $f-p$ curves are smooth whereas the RAS curve has distinct changes in the slope. Fig. 14(b), depicting the average number of contacts vs. penetration depth curve for Case 2 and for the RAS, clearly demonstrates how the number of the contacts changes from a jump function of penetration

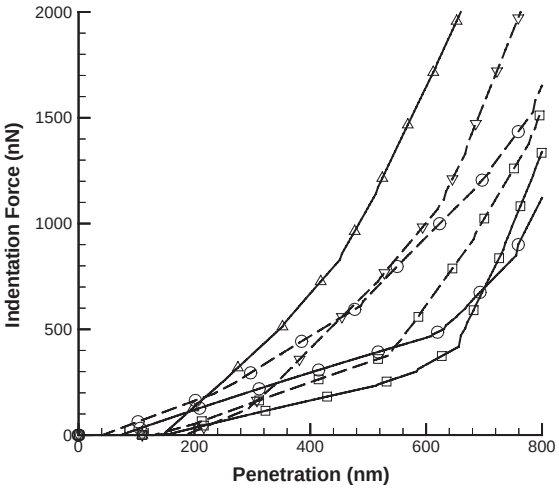

Fig. 13. Case 5: random nanoindentations on a VACNT forest where the nanotubes are randomly distributed, and have average length of 1100 nm with deviation of 20%, average diameter of 80 nm with deviation of 20%.

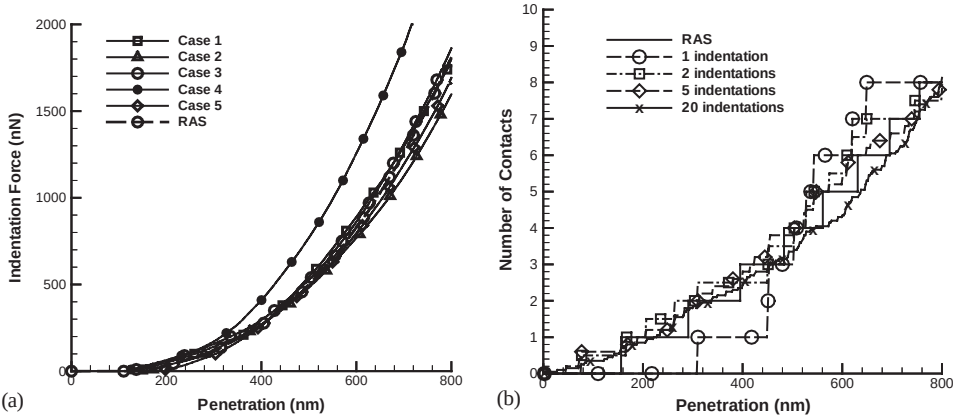

Fig. 14. (a) Average $f-p$ curves for Case 1–5; (b) Number of contacts vs. penetration depth curves from Case 2.

depth for an individual indentation to a continuous function over the average of 20 indentations.

The parametric study has demonstrated that a statistically representative $f-p$ indentation resistance curve can be obtained. Averaging the $f-p$ curves obtained from indentation at several locations provides a representation of the behavior of the VACNT even for a relatively sparse array with a 20% variation in CNT geometry. Therefore, experiments should be conducted at several locations and averaged in order to best

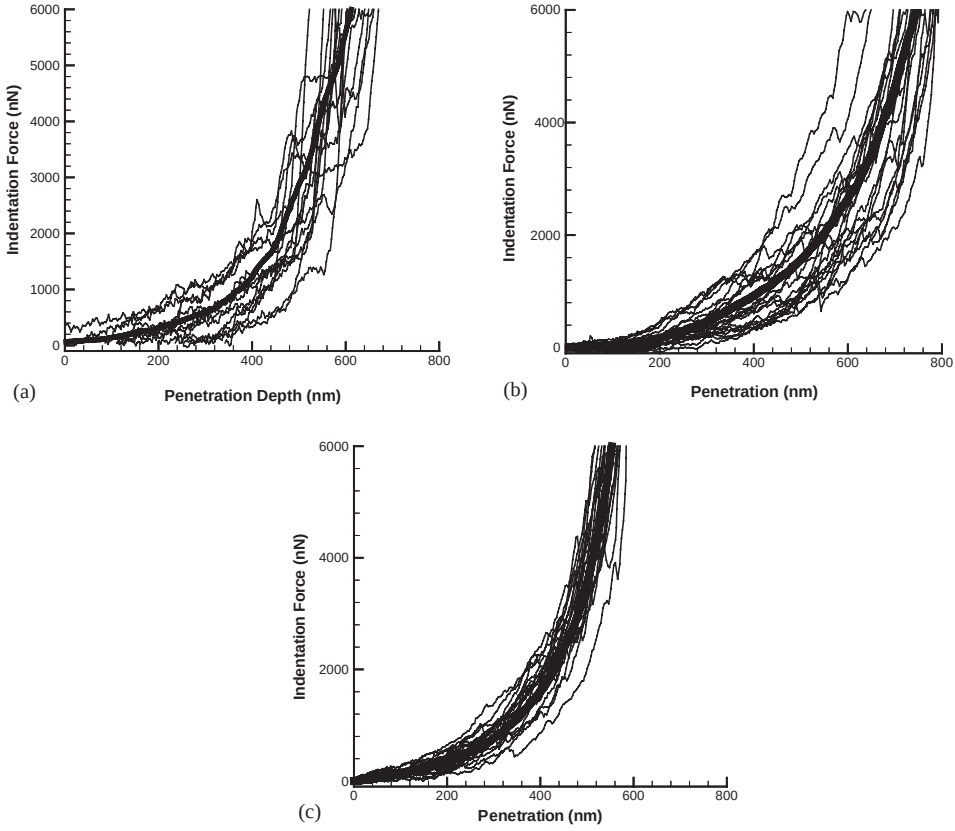

Fig. 15. Indentation force-penetration curves for (a) Sample A; (b) Sample B; and (c) Sample C. The thin solid lines are experimental curves; the thick solid lines are average curves.

represent the VACNT behavior; comparison with simulations can then be used to identify CNT properties.

4. Results and discussions

4.1. VACNT indentation

Nanoindentation tests were conducted on three VACNT forest samples, whose dimensions are listed in Table 1. In the experiment on each sample, more than 60 nanoindentations were executed at different locations, each of which was at least 800 nm away from another. The first 20 $f-p$ curves for each sample are shown in Fig. 15 (a)–(c), while the average curve for each VACNT is calculated over all experiments. Also note that repeated indentations at some random locations showed good repeatability when the indentation force is less than about 8000 nN, demonstrating both the elastic nature of the indentation and the repeatability of this measurement.

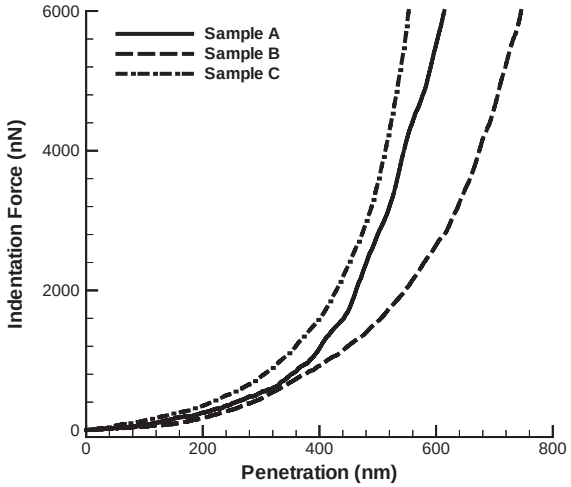

Fig. 16. Average $f-p$ curves for the three samples from experiments.

Fig. 15 shows the $f-p$ curves for 20 nanoindentation tests on each of the three samples, where the thick solid lines give the average experimental $f-p$ curves and the thin lines give the $f-p$ curves from the first 20 tests. Fig. 16 compares the average $f-p$ curves from the three samples. As discussed before, since Sample C has the highest nanotube areal density, the $f-p$ curves from Sample C show less scatter than those from Sample A and Sample B. Since Sample C has the largest areal density and smallest length, it has the highest indentation resistance. Although Sample A and Sample B have nearly the same areal density, Sample A has a larger average diameter and a smaller average length, resulting in a stiffer penetration resistance than that from sample B.

The theoretical models, together with numerical simulations, are now used to determine the effective bending stiffness $(EI)_{\text{eff}}$ of the nanotubes in each sample. In the model, both h_0 and $(EI)_{\text{eff}}$ are variables for optimization to minimize the deviation of the average of statistical simulations from the average of experimental results. Appendix A discusses the details on how to obtain the parameters $(EI)_{\text{eff}}$ and h_0.

Fig. 17 compares the average curves from statistical simulations and from experiments. Fig. 18 shows the $f-p$ curves from 20 simulated nanoindentations on the three samples, where the areal density, length, and diameters of nanotubes are generated statistically, following the data in Table 1. Table 2 lists the predicted effective bending stiffness for the three samples.

4.2. Determination of bending and axial modulus of constituent MWCNTs

The elastic modulus of the constituent nanotubes is now reduced from the measured $(EI)_{\text{eff}}$ using various approaches.

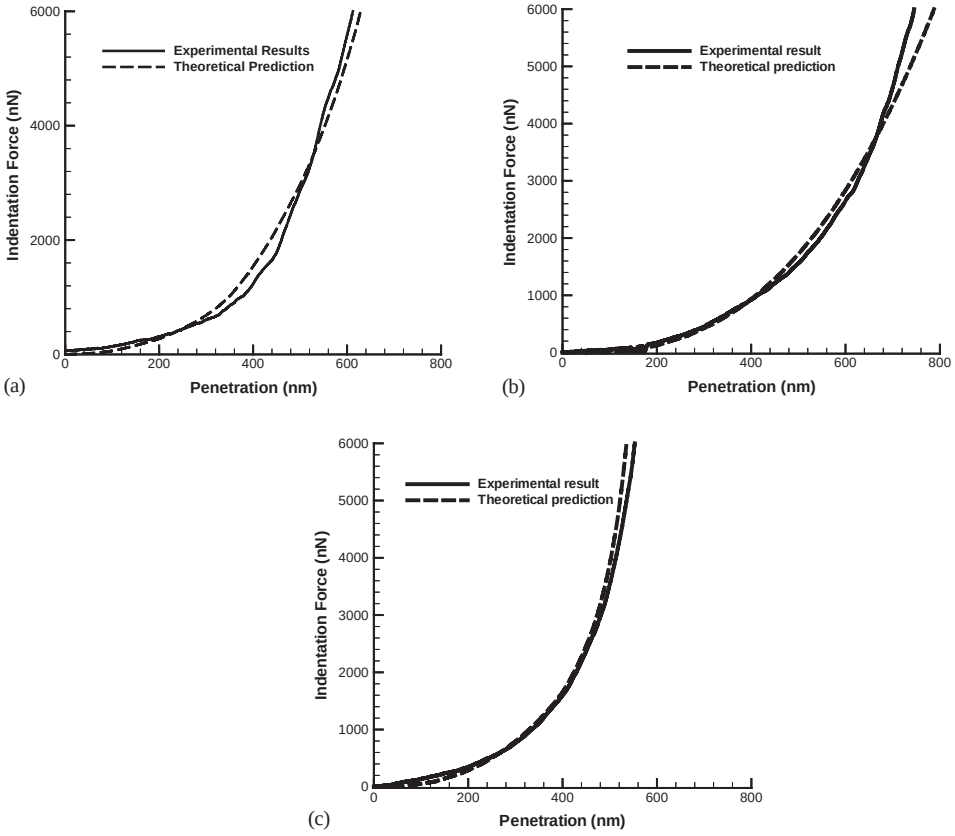

Fig. 17. The average curves from theoretical predictions and from experiments for (a) Sample A; (b) Sample B; and (c) Sample C.

An effective bending modulus E_t^{b} is estimated following the technique used by other investigators in experimental studies on isolated nanotubes. The effective bending modulus of the MWCNT, E_t^{b}, is calculated by dividing the measured effective bending stiffness, $(EI)_{\mathrm{eff}}$, by an effective moment of inertia, I_{eff}, which is assumed to be given by the outer diameter of the MWCNT D_{o},

$$E_t^{\mathrm{b}} = \frac{(EI)_{\mathrm{eff}}}{I_{\mathrm{eff}}} = \frac{64(EI)_{\mathrm{eff}}}{\pi D_{\mathrm{o}}^4}. \tag{10}$$

The effective bending modulus for samples A, B, and C are calculated to be 0.91, 1.24, and 1.14 TPa, respectively. These values are in good agreement with the values obtained by Wong et al. (1997) and by Salvetat et al. (1999). However, note that by using $(EI)_{\mathrm{eff}} = E_t^{\mathrm{b}} \times \pi D_{\mathrm{o}}^4/64$, important details of the nanotube structure are neglected.

To further verify the new method and investigate mechanical properties of nanotube structure, the multi-walled nature of the structure is considered in interpreting $(EI)_{\mathrm{eff}}$. A MWCNT consists of concentric walls of effective wall thickness t and inter-wall

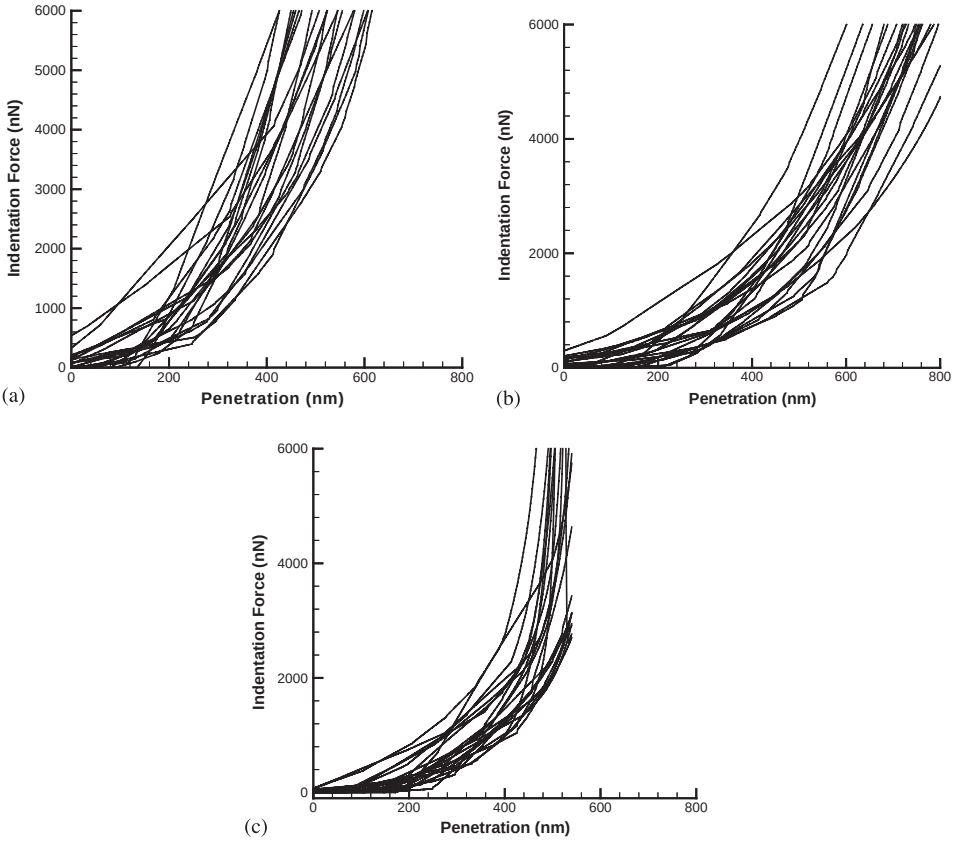

Fig. 18. Indentation force-penetration curves from 20 simulated nanoindentations on the three samples, where the areal density, length, and diameters of nanotubes follow the statistical data in Table 1. (a) Sample A; (b) Sample B; and (c) Sample C.

Table 2
Predictions of effective bending stiffness for the three VACNT samples

VACNT sample	$(EI)_{\text{eff}}(\text{N(nm)}^2)$
A	5.2
B	4.0
C	0.51

spacing s, as shown in Fig. 19. The walls maintain an inter-wall spacing of s due to normal van der Waals interaction. This separation is sustained during bending as observed in TEM (e.g., Poncharal et al., 1999). The shear interaction/stiffness between walls is observed to be very low (Cumings and Zettl, 2000; Yu et al., 2000). Indeed, this has led to proposals that CNTs be used as slider bearings (Cumings and Zettl, 2000; Kolmogorov and Crespi, 2000). These wall to wall interactions suggest that the

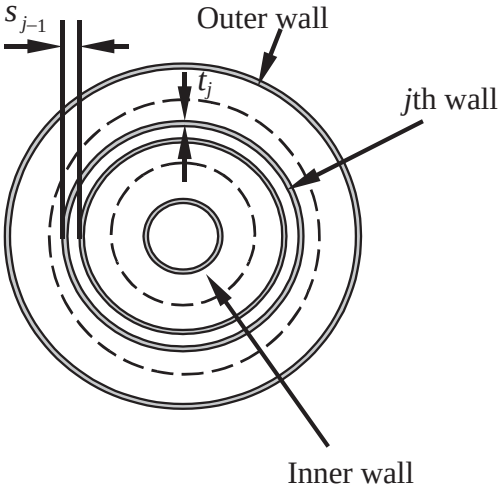

Fig. 19. Schematic of the cross section of the multiwalled structure of MWCNTs.

effective bending stiffness $(EI)_{\text{eff}}$ of the MWCNT can be well approximated through the sum of the bending stiffness of each tube. This summation approach has also been proposed by Govindjee and Sackman (1999).

For the jth wall, the moment of inertia I_j and cross sectional area A_j are given by

$$I_j = \frac{\pi}{64}[D_j^4 - (D_j^4 - 2t)^4], \tag{11a}$$

$$A_j = \frac{\pi}{4}[D_j^2 - (D_j - 2t)^2], \tag{11b}$$

where D_j is the outer diameter for the jth tube. The outer diameter of the (j-1)th wall is

$$D_{j-1} = D_j - 2s. \tag{12}$$

The total bending stiffness $(EI)_{\text{eff}}$ and axial stiffness $(EA)_{\text{eff}}$ of a MWCNT are then given by

$$(EI)_{\text{eff}} = \sum_{j=1}^{N} E_t^{\text{w}} I_j = E_t^{\text{w}} \sum_{j=1}^{N} I_j, \tag{13a}$$

$$(EA)_{\text{eff}} = \sum_{j=1}^{N} E_t^{\text{w}} A_j = E_t^{\text{w}} \sum_{j=1}^{N} A_j, \tag{13b}$$

where N is the number of walls, and E_t^{w} is the modulus of a tube wall and is taken to be identical for all walls in a CNT. Since $(EI)_{\text{eff}}$ is the bending stiffness measured in the test, the tube wall modulus E_t^{w} is obtained as

$$E_t^{\text{w}} = \frac{(EI)_{\text{eff}}}{\sum_{j=1}^{N} I_j}. \tag{14a}$$

Table 3
E_t^{b}, E_t^{w}, E_t^{a}, and N for the three samples

Sample	$(EI)_{\mathrm{eff}}$ (N(nm)^2)	E_t^{b} (TPa)	E_t^{w} (TPa)	E_t^{a} (TPa)	N
A	5.2	0.91	4.14	0.90	143
B	4.0	1.24	5.61	1.23	123
C	0.51	1.14	5.11	1.11	72

If the effective axial stiffness $(EA)_{\mathrm{eff}}$ of a nanotube is the summation of the axial stiffness of the N walls in the nanotube, then the effective axial Young's modulus E_t^{a} of a nanotube can be obtained as

$$E_t^{\mathrm{a}} = \frac{E_t^{\mathrm{w}} \sum_j^N A_j}{A_{\mathrm{t}}}, \tag{14b}$$

where A_{t} is the total cross sectional area, $A_{\mathrm{t}} = \pi D_{\mathrm{o}}^2/4$.

The inter-wall spacing, s, is set by the equilibrium spacing of the walls as determined by the van der Waals interactions, and values have been reported ranging from 0.34 to 0.39 nm (Saito et al., 1993; Sun et al., 1996; Kiang et al., 1998); here we take $s =$ 0.344 nm. The effective mechanical wall thickness has been determined by investigators by comparing atomistic level simulations and shell theory, e.g. Yakobson et al. (1996). Investigators suggest that the effective mechanical thickness of a nanotube wall range from $t \approx 0.066$ to 0.075 nm (see Pantano et al., 2003). The inner diameter of various VACNT structures is typically less than 10 nm, while the exact value of inner diameter should be determined from HRTEM. Nevertheless, from Eq. (11a), the inner tubes of diameter less than 10 nm contribute minutely to the total moment of inertia. Therefore, $D_{\mathrm{i}} \approx 6$ nm is used in current analysis. Using $D_{\mathrm{i}}=6$ nm, $t=0.075$ nm, and $s=0.344$ nm, we obtain the wall modulus, E_t^{w}, the tube axial modulus, E_t^{a}, and the average number of walls, N for each sample. Results are given in Table 3. These predictions are in good agreement with other theoretical and experimental reports, and verify the efficacy of the new method. For example, when using a mechanical thickness of 0.075 nm, atomistic simulations give a wall modulus of 4.8 TPa (see Pantano et al., 2003), which agrees well with predicted values of 4.14 to 5.61 TPa in Table 3.

5. Conclusions

Nanoindentation tests have been used to determine the mechanical properties of vertically aligned carbon nanotube (VACNT) forests and constituent carbon nanotubes. A study of the physical process of nanoindentation on VACNT forests reveals a process where nanotubes are consecutively bent during the penetration of the indentor. Unlike nanoindentation on homogenous materials, such as thin film coatings, where the elastic modulus and yield stress of coating materials are typically obtained, the resistance of VACNT forests to penetration is a result of superposition of the bending responses of nanotubes as the indentor successively encounters tubes in the forest. Nanoindentation tests, together with a micro-mechanical model using beam theory, were used to deter-

mine the effective bending stiffness $(EI)_{\text{eff}}$ of the MWCNT of the VACNTs studied. A simple method which accounts for the multiwalled structure of multiwall nanotubes was used to interpret the obtained $(EI)_{\text{eff}}$ in terms of the modulus of a nanotube wall E_t^{w}, and the effective axial modulus of a nanotube E_t^{a}.

Nanoindentation tests on three VACNT forest samples revealed the effective bending modulus of the MWCNTs to be $E_t^{\text{b}} = 0.91$–1.24 TPa, effective axial modulus to be $E_t^{\text{a}} = 0.9$–1.23 TPa, and the wall modulus to be $E_t^{\text{w}} = 4.14$–5.61 TPa, using a mechanical wall thickness of 0.075 nm. The good agreement of these predictions with other theoretical and experimental results supports the effectiveness of the new method.

The use of nanoindentation together with the proposed micromechanical model of the successive bending of nanotubes as the indentor penetrates into the forest is shown to provide a relatively easy measure of the bending stiffness, wall modulus and axial modulus of the constituent nanotubes. This new technique requires no special treatment of the samples, making it promising to apply this method to a large number of tests to determine the properties of CNTs in a statistical manner, which sometimes is more important than knowing properties for a few isolated nanotubes. The simplicity of the measurement suggests the potential use of this method as a quality control measurement in mass production. This proposed technique has been shown to be effective on VACNTs with random distributions of CNTs and would be even more effective on regularly patterned and more uniform VACNTs, where processes for producing such VACNTs are under investigations by several groups. For highly dense arrays, the model can be extended to account for the van der Waals interactions by monitoring the proximity of neighboring nanotubes during nanotube bending in much the same way as the interactions between nanoindentor and nanotubes were determined. The proposed nanoindentation and corresponding reduction of data are also applicable to vertically aligned nanofibers. Indentation of vertically aligned nanofibers is currently being investigated.

Acknowledgements

This research was funded in part by the CMI (Cambridge-MIT Institute) Project of Carbon Nanotube Enabled Materials, and in part by the AFOSR DURINT on Microstructure, Processing and Mechanical Performance of Polymer Nanocomposites (Air Force Contract No. F49620-01-1-0447).

Appendix A. Reducing $(EI)_{\text{eff}}$ and h_0

The parameter h_0 can be eliminated by scrutiny of the nanoindentation process using DI Dimension 3100 SPM. In such a nanoindentation, the output from the test is indentation force vs. piezo-scanner indentation movement (z movement) curve (f–z curve, which can be directly obtained from the raw output, photo detector voltage vs. z movement curve), which is constructed such that the indentation movement is measured backward starting from the point where the maximum indentation force is reached.

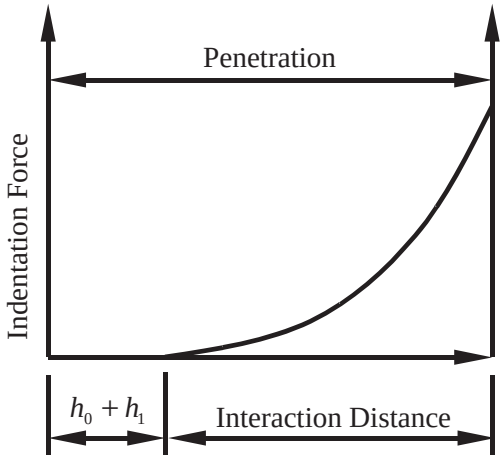

Fig. 20. Penetration and interaction distance.

It is therefore recognized that depending on where the maximum force is reached, the output f–z curve floats along the indentation direction. A force-penetration curve (Fig. 20) can be deduced from the f–z curve. In Fig. 20, we define the interaction distance as measuring the distance between the point where the indentor encounters the first nanotube and the point where the maximum indentation force is reached. Clearly, the penetration depth is distinct from the interaction distance by the amount of $h_0 + h_1$. As the number of tests increases, the difference between the average of interaction distance and the average penetration depths approaches $h_0 + \bar{h}_1$. The benefit of interaction distance is that h_0 falls at the end of interaction distance, making h_0 a trivial parameter.

Taking advantage of this feature, we proposed a method to determine $(EI)_{\text{eff}}$. The method requires to reconstruct all f–p curves from experiments and simulations, and starts with choosing a suitable reference indentation force f_0 and a reference position q^0. As discussed in Appendix B, a small value of f_0 should be used (in this paper, $f_0 = 4000$ nN is used for the three samples). We denote the ith f–p curve as $f_i = f_i(p_i)$, and $f_i(p_i^0) = f_0$. We then shift the ith curve so that $f_i(q^0) = f_0$, which can be obtained simply by a coordinate translation where $q_i = p_i + (q^0 - p_i^0)$. Such a process makes all the curves converge to a point where $f = f_0$ and $q = q^0$. The shifted curves are then averaged. The same process should also apply to curves from statistical simulations. The two averaged curves are compared and the final $(EI)_{\text{eff}}$ is determined such that the best agreement between the two averaged curves can be reached.

Appendix B. Bending deformation of a tube

From the free body diagram (Fig. 5), the moment at any point x along the tube is

$$M = -T_i x - P_i(w_0 - w). \tag{B.1}$$

Classical beam theory gives the relationship between moment and curvature (taking deflection and curvature to be related by $\kappa = \mathrm{d}^2w/\mathrm{d}x^2$) to be

$$(EI)_{\text{eff}} \frac{\mathrm{d}^2 w}{\mathrm{d}x^2} = T_i x + P_i(w_0 - w). \tag{B.2}$$

Although the nature of the bonding between nanotubes and substrate is not clear, SEM micrographs taken at the locations where tweezers swept over the surface show crater shape debris on the substrate, implying a strong connection between nanotubes and substrate. Therefore, it is reasonable to assume a clamped boundary condition at the end of the tube, e.g.

$$w|_{x=L} = 0 \quad \text{and} \quad \left.\frac{\mathrm{d}w}{\mathrm{d}x}\right|_{x=L} = 0. \tag{B.3}$$

Taking $k_i^2 = P_i/(EI)_{\text{eff}}$, and $y = w_0 - w$, Eqs. (B.2) and (B.3) can be written as

$$\frac{\mathrm{d}^2 y}{\mathrm{d}x^2} + k_i^2 y = -\frac{T_i x}{(EI)_{\text{eff}}}, \tag{B.4}$$

with boundary conditions

$$y|_{x=0} = 0 \quad \text{and} \quad \left.\frac{\mathrm{d}y}{\mathrm{d}x}\right|_{x=L} = 0. \tag{B.5}$$

The general solution to Eq. (B.4) is

$$y = A\cos k_i x + B\sin k_i x - \frac{T_i}{P_i} x, \tag{B.6}$$

where A and B are constants determined from Eq. (B.5),

$$A = 0 \quad \text{and} \quad B = \frac{T_i}{P_i k_i \cos k_i L}. \tag{B.7}$$

Therefore,

$$w = w_0 - \frac{T_i}{P_i k \cos k_i L} \sin k_i x + \frac{T_i}{P_i} x. \tag{B.8}$$

Since $w|_{x=L} = 0$,

$$w_0 = \frac{T_i}{P_i}\left(\frac{\tan k_i L}{k_i} - L\right), \tag{B.9}$$

and

$$w = \frac{T_i}{P_i k_i \cos k_i L}(\sin k_i L - \sin k_i x) - \frac{T_i}{P_i}(L - x). \tag{B.10}$$

The slope of the nanotube deformation is $-w'$, and

$$w' = \frac{T_i}{P_i}\left(1 - \frac{\cos k_i x}{\cos k_i L}\right). \tag{B.11}$$

Since the nanotubes are bent by the side surface of the indentor, the slope cannot exceed the slope of the side surface, or

$$-w' < \tan\theta. \tag{B.12}$$

If the inequality (B.12) is violated, the solution to this problem becomes complicated due to the change of the contact condition between the tube and the indentor from a point contact to a line contact. Nevertheless, a simple approximation to the solution can be realized using iterative method. Starting with Eq. (B.11), an effective length L' can be obtained with $-w'|_{x=L'} = \tan\theta$. This new L' and previous P_i are then used to calculate new k_i, P_i. This process will continue until inequality (B.12) is satisfied.

The occurrence of violation of inequality (B.12) depends on the nanoindentation location relative to the nanotube and usually is at large penetration depth. It should be noted that as penetration depth increases, the deflection of a nanotube could be so large that classical beam theory, which is based on small deformation assumption, will deviate from the true solution. The deformation at large penetration will be even more complicated by the increased possibilities of the interactions between nanotubes. Therefore, it is authors' suggestion that using above theory only for penetration depth less than about 70% of the average length of constituent CNTs.

References

Baughman, R.H., Zakhidov, A.A., de Heer, W.A., 2002. Carbon nanotubes—the route toward applications. Science 297, 787–792.

Chhowalla, M., Teo, K.B.K., Ducati, C., Rupesinghe, N.L., Amaratunga, G.A.J., Ferrari, A.C., Roy, D., Roberston, J., Milne, W.I., 2001. Growth process conditions of vertically aligned carbon nanotubes using plasma enhanced chemical vapor deposition. J. Appl. Phys. 90, 5308–5317.

Cumings, J., Zettl, A., 2000. Low friction nanoscale linear bearing realized from multiwall carbon nanotubes. Science 289, 602–604.

Digital Instrument, 1998. Nanoindentation and nanoscratching with SPMs, for NanoScope version 4.32 software. Support Note No. 225, Rev. F.

Govindjee, S., Sackman, J.L., 1999. On the use of continuum mechanics to estimate the properties of nanotubes. Solid State Commun. 110, 227–230.

Han, J.H., Lee, C.H., Jung, D.Y., Yang, C.W., Yoo, J.B., Park, C.Y., Kim, H.J., Yu, S., Yi, W., Park, G.S., Han, I.T., Lee, N.S., Kim, J.M., 2002. NH_3 effect on the growth of carbon nanotubes on glass substrate in plasma enhanced chemical vapor deposition. Thin Solid Films 409, 120–125.

Huang, Z.P., Xu, J.W., Ren, Z.F., Wang, J.H., Siegal, M.P., Provencio, P.N., 1998. Growth of large-scale well-aligned carbon nanotubes by plasma enhanced hot filament chemical vapor deposition. Appl. Phys. Lett. 73, 3845–3847.

Huang, Z.P., Wang, D.Z., Wen, J.G., Sennett, M., Gibson, H., Ren, Z.F., 2002. Effect of nickel, iron and cobalt on growth of aligned carbon nanotubes. Appl. Phys. A 74, 387–391.

Kiang, C.H., Endo, M., Ajayan, P.M., Dresselhaus, G., Dresselhaus, M.S., 1998. Size effects in Carbon Nanotubes. Phys. Rev. Lett. 81 (9), 1869–1872.

Kolmogorov, A.N., Crespi, V.H., 2000. Smoothest bearings: interlayer sliding in multiwalled carbon nanotubes. Phys. Rev. Lett. 85 (22), 4727–4730.

Pantano, A., Boyce, M.C., Parks, D.M., 2003. Mechanics of deformation of single and multiwalled carbon nanotubes. J. Mech. Phys. Solids, in press.

Poncharal, P., Wang, Z.L., Ugarte, D., de Heer, W.A., 1999. Electrostatic deflections and electromechanical resonances of carbon nanotubes. Science 283, 1513–1516.

Saito, Y., Yoshikawa, T., Bandow, S., Tomita, M., Hayashi, T., 1993. Interplayer spacing in carbon nanotubes. Phys. Rev. B 48 (3), 1907–1909.

Salvetat, J.P., Bonard, J.M., Thomson, N.H., Kulik, A.J., Forro, L., Benoit, W., Zuppiroli, L., 1999. Mechanical properties of carbon nanotubes. Appl. Phys. A 69, 255–260.

Sun, X., Kiang, C.H., Endo, M., Takeuchi, K., Furuta, T., Dresselhaus, M.S., 1996. Stacking characteristics of graphene shells in carbon nanotubes. Phys. Rev. B 54 (18), 12629–12632.

Treacy, M.M.J., Ebbesen, T.W., Gibson, J.M., 1996. Exceptionally high Young's modulus observed for individual carbon nanotubes. Nature 381, 678.

Wong, E.W., Sheehan, P.E., Lieber, C.M., 1997. Nanobeam mechanics: elasticity, strength, and toughness of nanorods and nanotubes. Science 277, 1971–1975.

Yakobson, B.I., Brabec, C.J., Bernholc, J., 1996. Nanomechanics of carbon tubes: instabilities beyond linear response. Phys. Rev. Lett. 76 (14), 2511–2514.

Yu, M.F., Yakobson, B.I., Ruoff, R.S., 2000. Controlled sliding and pullout of nested shells in individual multiwalled carbon nanotubes. J. Phys. Chem. B 104, 8764–8767.